Volume 12, Issue 1, December 2025 ISSN 2542-2545

The HIMALAYAN PHYSICS

A peer-reviewed Journal of Physics

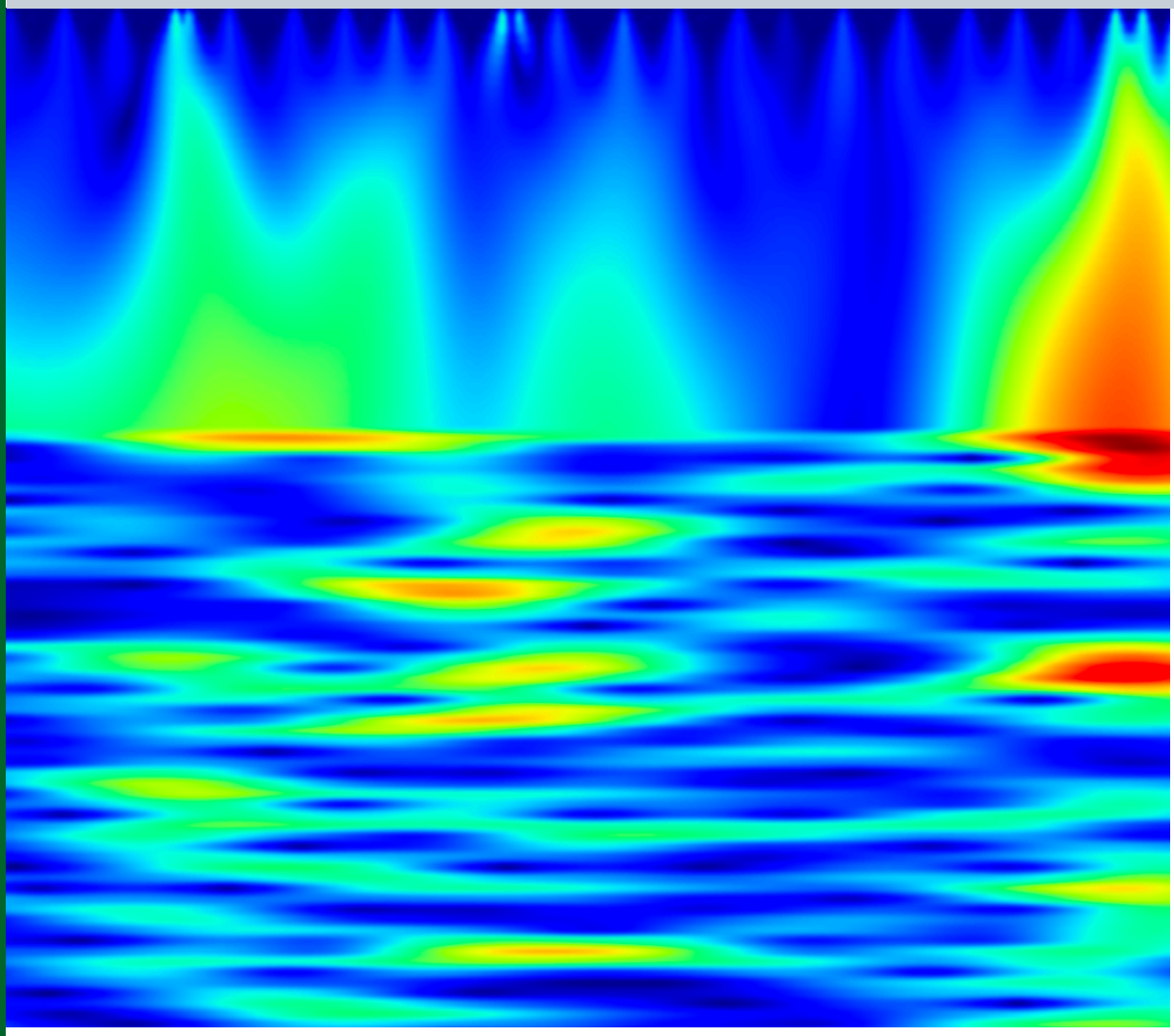

Department of Physics, Prithvi Narayan Campus, Pokhara
Nepal Physical Society, Gandaki Chapter, Pokhara

Publisher

Department of Physics, Prithvi Narayan Campus, Pokhara
Nepal Physical Society, Gandaki Chapter, Pokhara

The Himalayan Physics

Volume 12, Issue 1, December 2025

ISSN 2542-2545

The Himalayan Physics (HimPhys) is an open access peer-reviewed journal that publishes quality articles which make innovative contributions in all areas of Physics. HimPhys is published annually by Nepal Physical Society (Gandaki Chapter), and Department of Physics, Prithvi Narayan Campus, Pokhara. The goal of this journal is to bring together researchers and practitioners from academia in Nepal and abroad to focus on advanced techniques and explore new avenues in all areas of physical sciences and establishing new collaborations with physics community in Nepal.

Chief Editor

Aabiskar Bhusal

Cover: Wavelet time–frequency representation for the NEAR condition. The figure shows stronger low-frequency activity over time, suggesting greater mental effort and engagement when surrounding stimuli are close to the target. (Figure 3(a), Himalayan Physics 12, 1-14, (2025))

Volume 12, Issue 1, December 2025 ISSN 2542-2545

The HIMALAYAN PHYSICS

A peer-reviewed Journal of Physics

Publisher

Department of Physics, Prithvi Narayan Campus, Pokhara

Nepal Physical Society, Gandaki Chapter, Pokhara

Nepal Physical Society

Gandaki Chapter

Pokhara, Nepal

Himalayan Physics Vol-12(1) (2025)

TABLE OF CONTENTS

****

Him. Phys. **12** 64-82, (2025) ISSN: 2542-2545

Himalayan Physics

Molecular insights into Herniarin: Structural, spectroscopic, electronic and thermodynamic characterization via density functional theory

https://doi.org/10.3126/hp.v12i1.86388

Dipak Thapa[1, 3], Krishna Bahadur Rai[1, 2, 3*], Bishal Pandey[1], Madhav Prasad Ghimire[2†]

1 Department of Physics, Patan Multiple Campus, Lalitpur, Tribhuvan University, Nepal

2 Central Department of Physics, Tribhuvan University, Kirtipur, Nepal

3 These authors contributed equally.

Abstract: Density Functional Theory calculations at the B3LYP/6-311++G(d,p) level were performed to explore the structural, electronic, vibrational, and thermodynamic properties of Herniarin. The optimized geometry confirms molecular polarity and shows good agreement with experimental data for coumarin derivatives. Vibrational analysis verified the characteristic stretching and bending modes, while non-covalent interaction and Reduced Density Gradient analyses indicated weak van der Waals interactions without hydrogen bonding. Electron localization analyses revealed pronounced localization around heteroatoms and delocalization within the aromatic framework. Frontier molecular orbital and density of states analysis demonstrated a moderate energy gap, suggesting chemical stability. Reactivity descriptors indicated balanced stability and reactivity, and electrostatic potential maps identified oxygen and hydrogen atoms as the primary reactive sites. Thermodynamic properties exhibited systematic temperature dependence with strong correlations, confirming the thermal stability and predictable behavior of the molecule.

Keywords: Herniarin • Density functional theory • Optimized molecular structure • Vibrational analysis • Electronic properties • Thermodynamic properties

Received: 2025-11-12 **Revised: 2025-12-14** **Published: 2025-12-20**

I. Introduction

Herniarin is a naturally occurring methoxy-substituted coumarin, also described as a methylated derivative of umbelliferone [1]. Coumarin, a colorless benzopyrone phytochemical, is widely distributed in fruits, leafy vegetables, and herbs [2, 3] and exhibits diverse pharmacological properties, including anti-inflammatory, anticoagulant, antioxidant, antimicrobial, and antitumor effects. Herniarin is a planar molecule with the IUPAC name 7-methoxychromen-2-one and molecular formula $C_{10}H_8O_3$ [4]. It was first

* *Corresponding Author: krishnarai135@gmail.com*
† *Corresponding Author: madhav.ghimire@cdp.tu.edu.np*

isolated from Herniaria species [1] and later identified in Equisetum debile Roxb. [5], Lavandula officinalis [6], and several plant families such as Caryophyllaceae, Gramineae, Labiatae, Leguminosae, Moraceae, Rosaceae, Rutaceae, Solanaceae, and Compositae [7]. Structurally, herniarin contains ten carbon atoms: nine sp^2-hybridized carbons forming the aromatic chromen-2-one ring and one methoxy carbon (C1), while the carbonyl carbon (C12) belongs to the α-pyrone moiety [5, 6]. Previous computational studies on related methoxycoumarins have demonstrated the effectiveness of Density Functional Theory (DFT) in elucidating structural, electronic, and spectroscopic properties. For instance, DFT analyses of 7-methoxy-4-bromomethyl coumarin reported geometrical parameters consistent with related coumarins, shorter C-O bond lengths due to benzene-α-pyrone fusion, and HOMO-LUMO electron density localized mainly on the parent ring and methoxy group [8]. Studies on 3-acetyl-methoxycoumarin further revealed charge transfer from carbon to oxygen atoms, increasing the double-bond character of the carbonyl group [9], while studies on 7-methoxycoumarin reveal, the benzene ring in 7-methoxycoumarin retains aromaticity similar to benzene and methoxybenzene, while the fused α-pyrone ring shows mild aromatic character from π-electron and oxygen lone-pair delocalization [10].

Despite extensive investigations of coumarins, herniarin has not been systematically studied using DFT with respect to its optimized geometry, vibrational characteristics, electronic structure, and thermodynamic properties, particularly at the B3LYP/6-311++G(d,p) level combined with GaussSum 3.0.2 and Moltran software. Addressing this gap is important because the structural and electronic features of herniarin are expected to influence its reactivity, spectroscopic behavior, and potential pharmacological or toxicological applications. In this work, comprehensive DFT calculations are performed to determine the optimized geometry, vibrational frequencies, and non-covalent interactions of herniarin using Reduced Density Gradient (RDG) analysis. The electronic structure is further examined through HOMO-LUMO analysis, Density of States (DOS), global reactivity descriptors, Molecular Electrostatic Potential (MEP), Electrostatic Potential (ESP) surfaces, Electron Localization Function (ELF), and Localized Orbital Locator (LOL). Mulliken atomic charges, electron density distribution, and thermodynamic properties are also evaluated, providing a theoretical foundation for spectroscopic identification, reactivity prediction, and potential applications in pharmacology and materials science.

II. Computational Methodology and Theoretical Details

Herniarin's calculations were performed using Gaussian 09W with the DFT/B3LYP method and the 6-311++G(d,p) basis set [11] and GaussView software [12] was used to visualize the molecular structures. The optimized structural parameters were used for vibrational frequency calculations to characterize the vibrational modes, along with analyses of HOMO-LUMO, global reactivity parameters, MEP, ESP, ED and Mulliken charges. The DOS spectrum was observed with the help of the GaussSum 3.0 program [13].

Iso-surface maps of NCI-RDG, ELF and LOL were generated using Multiwfn software version 3.8 [14] and Visual Molecular Dynamics (VMD) version 1.9.4a53 and gnuplot 6.0 software [15]. The thermodynamic parameters were obtained from the Moltran Program [16].

This study employed the RDG scatter plot and corresponding isosurface to depict and analyze non-covalent interactions. The RDG analysis is derived based on the following mathematical expression [17],

$$RDG(r) = \frac{1}{2(3\pi^2)^{\frac{1}{3}}} \frac{|\nabla\rho(r)|}{\rho(r)^{\frac{4}{3}}} \tag{1}$$

Where, $\nabla\rho(r)$ represents the gradient of the electron density ρ(r) at a given point within the molecule structure.

Topological analysis encompassing Electron Localization Function (ELF) calculation is obtained by the following equation [18],

$$ELF = \frac{1}{1 + \left(\frac{D}{D_h}\right)^2} \tag{2}$$

With $D = \frac{1}{2}\sum_i |\varphi_i|^2 - \frac{1}{8}\frac{|\nabla\rho|^2}{\rho}$ and $D_h = \frac{3}{10}\left(3\pi^2\right)^{\frac{2}{3}}\rho^{\frac{5}{3}}$, where D stands for excess kinetic energy and D_h represents its corresponding reference value.

The LOL analysis is determined using the Schmider and Becke formulation [19] and this LOL function is given by

$$LOL(r) = \frac{\tau(r)}{1 + \tau(r)} \tag{3}$$

Where τ(r) represents a dimensionless variable and defined by

$$\tau(r) = \frac{g_0(r)}{g(r)} = \frac{D_0(r)}{\frac{1}{2}\sum_i \eta_i |\nabla\varphi_i(r)|^2} \tag{4}$$

Here, g(r) denotes the electron kinetic energy, ϕ_i refers to the Hartree-Fock orbitals, and $D_\circ$(r) represents the value for a spin-polarized system.

Likewise, global reactivity parameters, including electron affinity (A), ionization potential (I), electronegativity (χ), chemical hardness (η), chemical potential (μ), chemical softness (S), and electrophilicity index (ω), were calculated from HOMO-LUMO energies using Koopmans' theorem [20, 21] such that:

$$I = -E_{\mathrm{HOMO}} \tag{5}$$

$$A = -E_{\mathrm{LUMO}} \tag{6}$$

Where I and A are the ionization potential and electron affinity, respectively.

Similarly, the hardness (η) of the molecule is defined as

$$\eta = \frac{I - A}{2} \tag{7}$$

The chemical potential (μ) is

$$\mu = -\frac{I + A}{2} \tag{8}$$

The chemical softness is the reciprocal of the chemical hardness

$$S = \frac{1}{\eta} \tag{9}$$

The electronegativity (χ) of the molecule is given by the equation

$$\chi = \frac{I + A}{2} \tag{10}$$

The Electrophilicity index (ω) is obtained as

$$\omega = \frac{\mu^2}{2\eta} \tag{11}$$

III. Result and Discussions

Geometrical Optimization

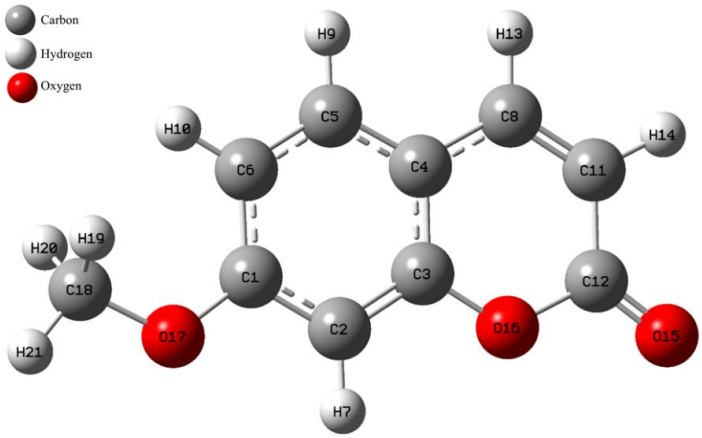

Figure 1. Optimized molecular structure with numbering atoms of Herniarin molecule.

Fig. 1 shows the optimized structure of Herniarin ($C_{10}H_8O_3$) molecule using DFT at the B3LYP/6-311++G (d, p) basis set, with atomic numbering and symbols. The optimized energy for this molecule is -16645.48 eV. In this calculation, it revealed that the dipole moment of molecule is 6.57 Debye.

Bond length, Bond angle and Dihedral angle

The calculated bond lengths range from 1.08 to 1.45 Å. The C-C bond lengths fall between 1.35 and 1.45 Å, in good agreement with experimental values of 1.36-1.39 Å, while all C-H bond lengths are approximately 1.08 Å, close to the experimental value of 1.07 Å[8, 22]. The O15-C12 bond length is 1.20 Å, consistent with reported values for comparable coumarin compounds. The ring C-O bond lengths (C12-O16 at 1.40 Å and C3-O16 at 1.36 Å) are shortened due to fusion of the benzene and α-pyrone rings [8]. The C11-C12 is the longest bond length (1.45 Å) and deviates +0.17 Å from the average (1.28 Å), indicating a significantly elongated bond, which may be due to weaker bonding, steric effects, or partial single-bond character. Whereas the C6-H10, C2-H7, C18-H21, C11-H14, C8-H13, C5-H9 bonds are the shortest bond length (1.08 Å), which deviates -0.20 Å from the average, indicating a strongly contracted bond, typically associated with higher bond order (e.g., double-bond character) or stronger orbital overlap. The C-C-C bond angles within the ring range from 117.47° to 121.64°, compared with experimental values of 118.48°-121.16°. The C-C-O ring bond angles lie between 115.99° and 126.47°, comparable to experimental values of 16.96°-122.09° [22]. The C12-O16-C3 bond angle is 122.91°, while C-C-H bond angles range from 115.64° to 122.77°, and the average H-C-H angle is 109.49°. Most dihedral angles fall within ±179-180°, indicating an almost fully planar molecular geometry. This planarity promotes π-electron delocalization across the aromatic system, consistent with the observed HOMO distribution and enhanced conjugation stability. For detailed numerical data, Table S1 summarizes the bond lengths, bond angles, and dihedral angles of the molecule in the supplementary material.

Vibrational analysis

Fig. 2 displays the infrared (IR) spectra of the title molecule that is captured over the range of 0-3500 cm^{-1}. The y-axis on the infrared graph shows the proportion of light transmitted, while the x-axis shows the wavenumber. The spectrum reveals a variety of vibrational modes, which occur due to the interaction between the material and infrared light specifically because the frequency and wavelength of IR radiation correspond to molecular vibrations [23–25]. The molecule consists of 21 atoms and 57 ($3N$-6) modes of vibrations. Different major modes of vibrations seen in the molecule are 20 stretching (valence bond vibrations) including symmetrical vibrations, 19 bending (deformation vibrations), and 18 torsion including out-plane vibrations.

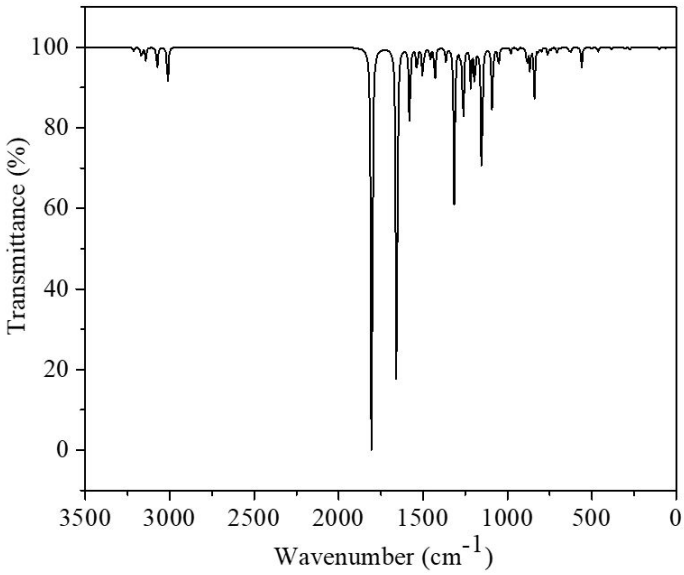

Figure 2. FT-IR-spectra of Herniarin using the DFT method.

C-H Vibrations

The C-H stretching vibrations are observed at 3012.53, 3075.08, 3142.18, and 3216.35 cm^{-1}. The C-H in-plane rocking and scissoring modes appear at 1537.03, 1430.31, and 1262.58 cm^{-1}, and at 1503.20 and 1493.57 cm^{-1}, respectively. The out-of-plane twisting and wagging vibrations are observed at 799.00 and 840.61 cm^{-1}, and at 940.39 and 997.26 cm^{-1}, respectively. All calculated C-H vibrational frequencies fall within the characteristic ranges reported for coumarin derivatives, with stretching modes occurring at 3100-3000 cm^{-1} and out-of-plane modes in the 1000-700 cm^{-1} region [8, 26].

C-C and C=C Vibrations

The C=C stretching vibrations typically occur in the range of 1650-1400 cm^{-1}, while C-C stretching vibrations are expected between 1420 - 1350 cm^{-1} [8, 22]. In the FTIR spectrum of the title molecule, these vibrations are observed at 1658.27, 1652.46, 1579.95, and 1364.63 cm^{-1}, confirming good agreement with standard values.

C=O Vibrations

The carbonyl (C=O) stretching vibration is generally observed in the 1780-1643 cm^{-1} region [9, 26]. For the title molecule, this vibration appears at 1803.62 cm^{-1}, which is close to the reported range for coumarin derivatives.

C-O Vibrations

C-O stretching vibrations are expected in the 1300-934 cm^{-1} region [8, 27]. The corresponding vibrations for the title molecule are observed at 1315.14, 1052.94, and 884.71 cm^{-1}, indicating consistency with standard vibrational assignments.

Aromatic C=C Ring Vibrations

Aromatic C=C ring stretching vibrations typically appear in the 1625-1400 cm^{-1} range [22]. The observed frequencies at 1364.63, 1579.95, 1652.46, and 1658.37 cm^{-1} fall within or close to this region, confirming the presence of conjugated aromatic ring vibrations.

Non-covalent interaction (NCI) - Reduced density gradient (RDG) analysis

The NCIs are examined through the scatter plot of the Reduced Density Gradient (RDG) versus sign($\lambda_2\rho$), where λ_2 is the second eigenvalue of the electron density Hessian matrix. This plot provides crucial insights into the nature and strength of non-covalent interactions across different regions of the molecule. The RDG iso-surface map and scatter graph's red zone ($\rho(r)>0$) together with red spikes signifies high level of steric repulsion between the atoms, green zone represents weak Van der Waals interactions observed around smaller sign($\lambda_2\rho$) values and the spikes in the green region imply that the atoms in the molecule have weak Van der Waals interactions. The blue region ($\rho(r)<0$) together with the spikes represents strong attractive hydrogen bonding or electrostatic interactions [17, 28].

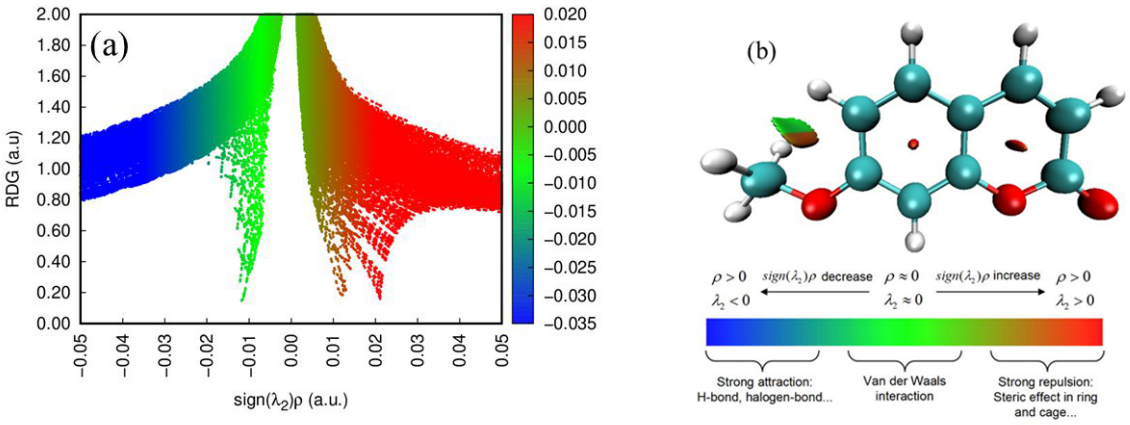

Figure 3. (a) RDG scatter plots and (b) Non-covalent interactions (NCI) plot of Herniarin molecule.

Fig. 3(a) presents the RDG iso-surface analysis, and it has been observed that there is strong involvement of steric repulsions (red spike), and van der Waals interactions (green spike) within the molecule [28, 29]. However, the absence of blue spikes indicates that there are no hydrogen bonding interactions. Fig. 3(b) represents the NCI analysis of the title molecule in which the red color disk/spindle

indicates the strong repulsive interaction (steric interaction) in middle of the aromatic rings together with red colour half disk in the region of O17, C1 and C18. The green colour half disk scattered around the molecule show the weak Van der Waals interaction which is due H10, H19, H20 and C18 atoms in the molecule. The absence of blue disk/spindle/blocks suggests no H-bond interaction between the atoms of the molecule.

Electron localization function (ELF) and Localized orbital locator (LOL)

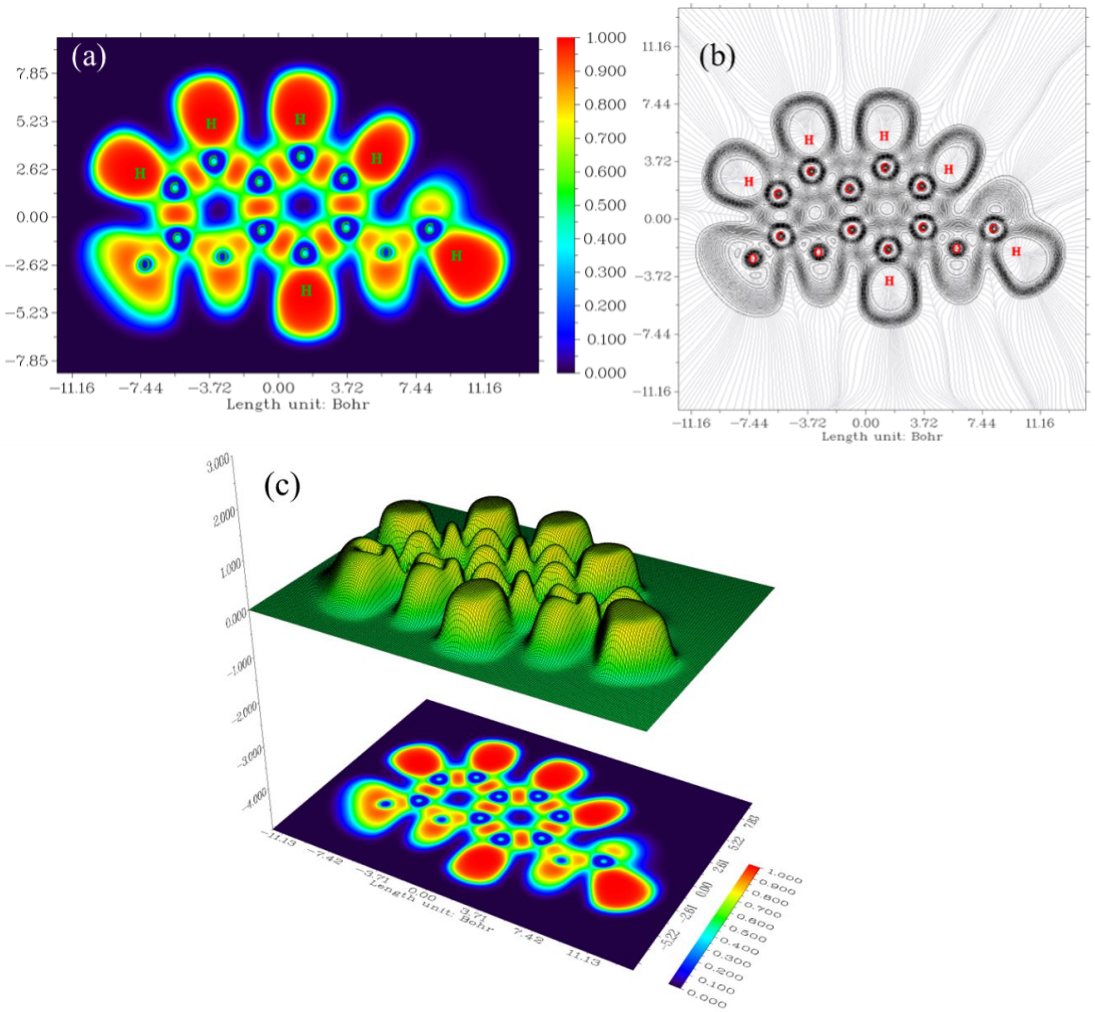

Figure 4. Electron Localization Function (a) Colored filled map, (b) Contour map, (c) Relief map with the 3D projection of shaded surface map depicting an electronic environment.

The ELF maps provide a clear picture of electron localization in Herniarin. In the filled color map (Fig. 4a), highly localized electron regions appear in red, particularly around the oxygen atom and the C-H bonding regions, reflecting concentrated bonding and lone-pair electron density. In contrast, the blue regions around the aromatic ring indicate electron delocalization within the π-system [30]. The con-

tour representation (Fig. 4b) further highlights these features, with densely packed contour lines around heteroatoms and C-H bonds confirming strong localization, while more diffuse patterns across the ring correspond to delocalized electrons [31]. The 3D relief projection (Fig. 4c) shows localization peaks near electronegative atoms and bonding regions, consistent with the filled and contour maps [32]. Together, these plots indicate that Herniarin possesses a localized electron environment around heteroatoms and σ-bonds, while maintaining delocalized π-electron character across the aromatic framework.

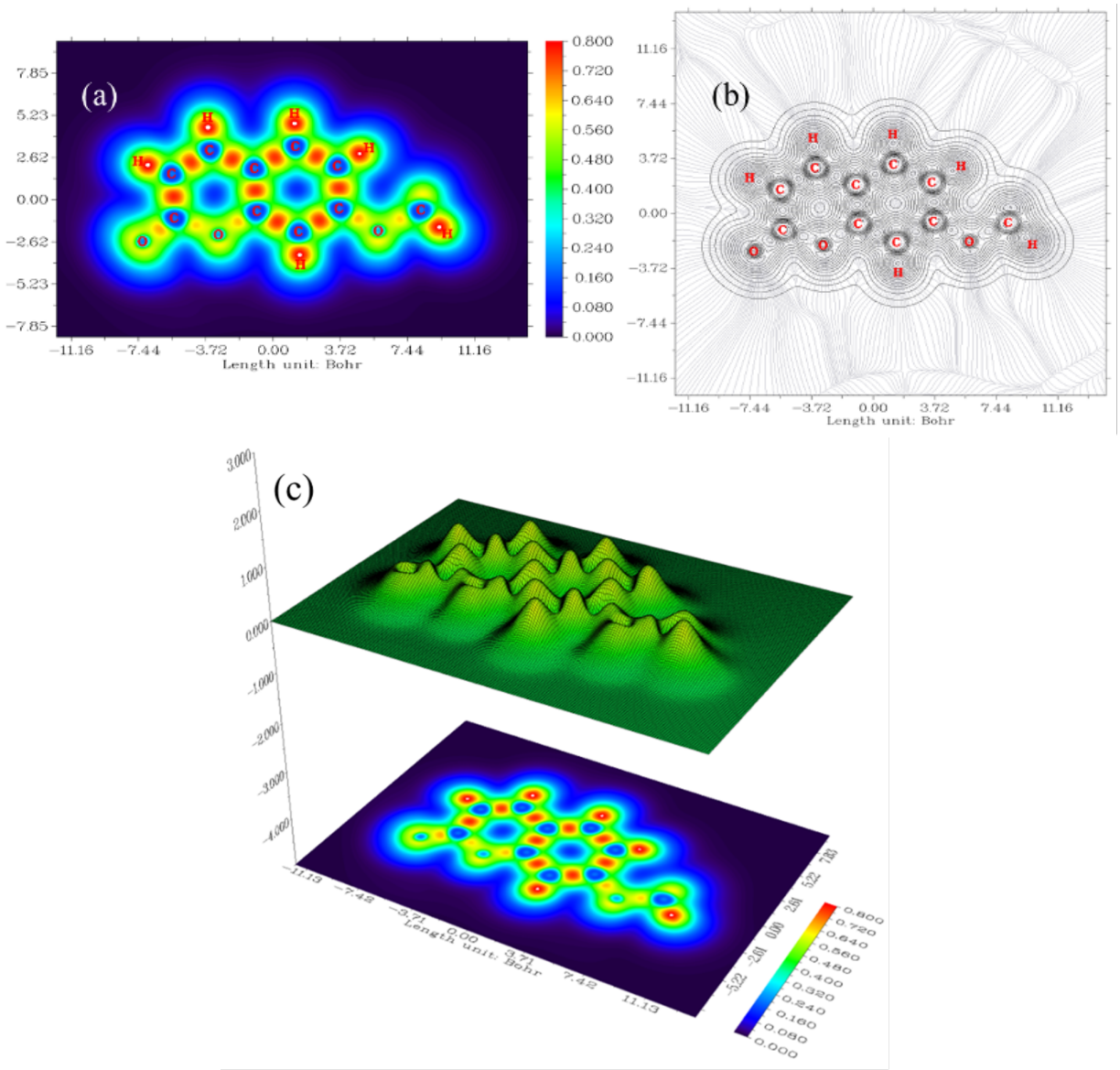

Figure 5. Localized orbital locator (a) colored filled map, (b) contour map, (c) 3D projection of shaded surface map depicting an electronic environment.

The LOL plots display a localization pattern similar to the ELF analysis. In the filled map (Fig. 5a), high localization appears as intense red/white regions centered on hydrogen atoms and along covalent

bonds, marking strong bonding interactions. The red regions between C-C atoms correspond to bond critical points, while blue zones across the ring indicate inner electron density with minimal localization [33]. In the contour map (Fig. 5b), the carbonyl group generates reduced localization around the C=O bond, whereas tightly spaced contours around C-H regions confirm strong localized electron density. The 3D shaded surface (Fig. 5c) shows pronounced peaks at hydrogen atoms and in bonding regions, illustrating high LOL values consistent with strong electron localization [34]. Lower regions on the surface correspond to delocalized regions across the aromatic ring [34, 35].

Frontier orbitals analysis

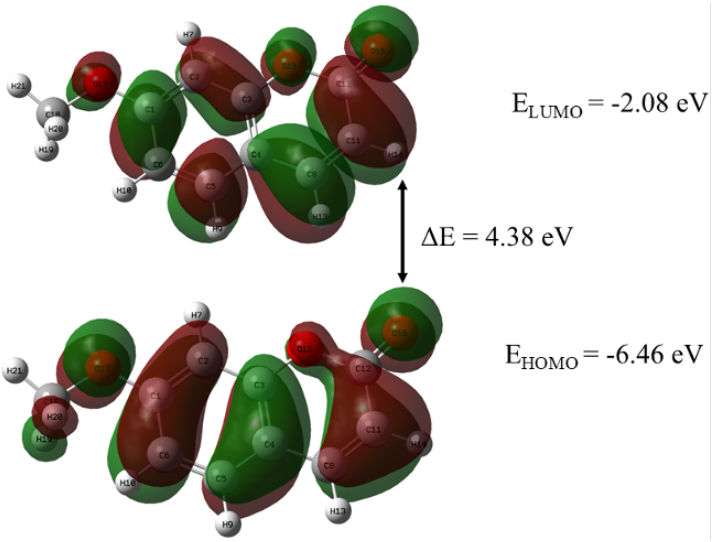

Figure 6. HOMO-LUMO orbitals of Herniarin.

The Highest Occupied Molecular Orbital (HOMO) represents the nucleophilic region, acting as an electron donor, whereas the Lowest Unoccupied Molecular Orbital (LUMO) corresponds to the electrophilic region and functions as an electron acceptor. The energy difference between these two orbitals, known as the HOMO-LUMO energy gap, is an important parameter for assessing molecular stability, reactivity and electronic transitions [36]. A smaller HOMO-LUMO gap generally indicates lower stability and higher chemical reactivity, while a larger energy gap implies greater stability and reduced reactivity [37]. According to Frontier Molecular Orbital (FMO) theory, transition states arise from interactions between the HOMO and LUMO of the reacting species, and a lower energy gap facilitates electronic transitions, whereas a higher gap suppresses them [38]. Fig. 6, illustrates the frontier molecular orbitals of the molecule. The HOMO and LUMO energies are calculated to be -6.46 eV and -2.08 eV, respectively, resulting in an energy gap ($\Delta E = E_{HOMO} - E_{LUMO}$) of 4.38 eV. This relatively wide energy gap indicates good chemical stability and comparatively low reactivity.

Density of states (DOS)

Fig. 7, represents the density of states (DOS) spectrum of the herniarin molecule, generated using the GaussSum 3.0 program [13]. The DOS provides essential insight into the electronic structure and overall electrical characteristics of the molecule. It highlights the contribution of electrons to the valence and conduction bands and is used to describe electronic excitation from the ground state to the lowest unoccupied energy band [39]. DOS analysis facilitates visualization of energy band formation and electron occupation. Positive DOS values indicate bonding interactions, negative values correspond to antibonding interactions, and zero values represent the absence of bonding interactions [40, 41]. In Fig. 7, the green-colored energy region represents the occupied (filled) donor orbitals, while the red-colored energy region corresponds to the virtual (unfilled) acceptor orbitals. The figure also shows that the herniarin molecule has an energy gap of 4.30 eV, which closely agrees with the 4.37 eV value obtained from the HOMO-LUMO analysis.

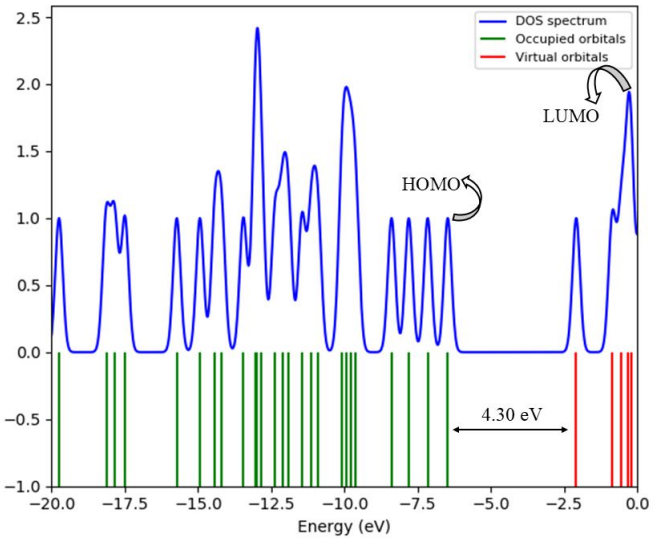

Figure 7. Density of states (DOS) spectrum of Herniarin molecule.

Global reactivity parameters

This study provides a variety of chemical reactivity parameters and information on the molecular structure's stability, aimed at enhancing our understanding of the properties of herniarin. The global reactivity indices considered in this study include electron ionization potential (I), electron affinity (A), chemical hardness (η), chemical potential (μ), chemical softness (S), electronegativity (χ), and electrophilicity index (ω), all of which are calculated here using Koopmans' theorem [20, 21]. The values for Ionization Potential ($I = -E_{HOMO}$) and Electron Affinity ($A = -E_{LUMO}$) are found to be 6.46 eV and 2.08 eV, respectively, for herniarin. The energy required to remove an electron from a gaseous atom is

known as ionization energy (I), whereas the energy released when an electron is added to a neutral atom or molecule to generate a negative ion in the gaseous state is known as electron affinity (A) [42, 43]. The chemical hardness (η) is found to be 2.19 eV, reflecting the molecule's stability and resistance to variations in electron density. The calculated chemical potential ($\mu = -4.27$ eV) represents the substance's potential energy, and a more negative value denotes a greater tendency to release energy or react [42]. The inverse of the global hardness is chemical softness, which indicates how readily a molecule can gain or lose an electron [24]. The calculated chemical softness ($S = 0.45$ eV^{-1}) reflects the molecule's polarizability and ability to facilitate electron transfer. The calculated electronegativity ($\chi = 4.27$ eV) represents the tendency of an atom to attract electrons within a chemical bond. The molecule's ability to accept electrons in chemical processes is indicated by its electrophilicity index (ω), which is found to be 4.16 eV [43].

Molecular electrostatic potential (MEP), Electrostatic potential (ESP), and Electron density (ED)

Fig. 8(a) shows the distribution of the molecular electrostatic potential (MEP), ranging from -6.185×10^{-2} a.u. (red) to 6.185×10^{-2} a.u. (blue). This plot provides an overview of the relative polarity of the title molecule and relates the values to electron density. The MEP at a given point around a molecule represents the net electrostatic effect produced by the combined charge distribution of its electrons and nuclei at that location [44]. Areas with a negative electrostatic potential are represented by red and yellow, whereas areas with a positive electrostatic potential are shown in blue [45]. In Fig. 8(a), the red region, representing negative electrostatic potential (electron-rich areas), is located mainly around O15, with a light-yellow gradient around O16 and O17, attributable to their lone pairs of electrons [45], indicating that O15, O16, and O17 of herniarin have higher energy levels. CH_3, H7, H9, H10, H13, and H14 comprise the majority of the light blue region, which represents positive electrostatic potential (electron-deficient areas) of herniarin. This indicates that the hydrogens in this region are at a lower energy level and are thus more susceptible to nucleophilic attack, making it an electron-acceptor region.

Fig. 8(b) shows the electrostatic potential mapped onto the molecular surface, emphasizing reactive sites and charge distribution, ranging from -1.284×10^{-2} a.u. (red, indicating electrophilic regions) to 1.284×10^{-2} a.u. (blue, indicating nucleophilic regions). Negative electrostatic potential is observed in the red area around O15 and the light-yellow gradient surrounding O16 and O17, suggesting that oxygen's high electronegativity pulls electron density to create a negative zone [46], whereas the rest of the surface exhibits a localized positive potential, indicating regions susceptible to nucleophilic attack. An electron density surface map, often combined with electrostatic potential visualization, provides detailed information on the molecule's size, shape, charge distribution, and reactive regions. As shown in Fig. 8(c), the map depicts a uniform charge distribution and indicates the probability of electron presence at

specific locations within the molecule.

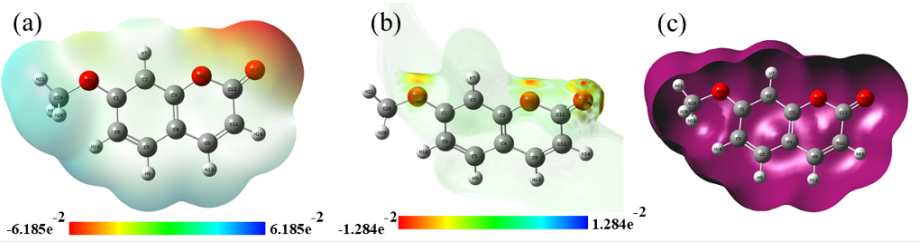

Figure 8. (a) Molecular electrostatic potential (b) Electrostatic potential, and (c) Electron density of Herniarin.

Mulliken atomic charge

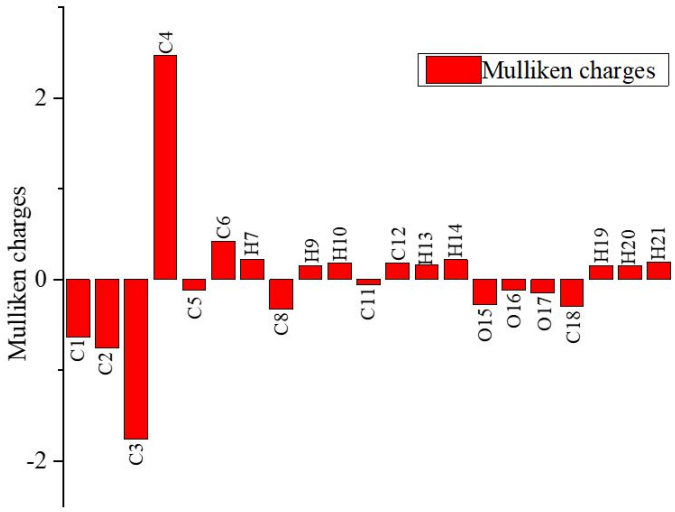

Figure 9. Histogram of Mulliken charges distribution of Herniarin molecule.

Mulliken atomic charge is a method for determining partial charges on atoms in a molecule by partitioning electron density according to the principles of Mulliken population analysis. Atoms receive charges based on the distribution of their electrons. Mulliken charges facilitate quantum calculations by influencing molecular characteristics, including electronic structure, polarizability, and dipole moment [47]. Fig. 9, shows a histogram of the Mulliken charge distribution for each atom of the title molecule. It is observed that all hydrogen atoms are positively charged, and all oxygen atoms are negatively charged. For the carbon atoms, C1, C2, C3, C5, C8, C11, and C18 possess negative charge distributions, whereas C4, C6, and C12 show positive charge distributions. Among them, it is clear that C4 and C3 have the highest positive and negative charges, respectively.

Thermodynamic Analysis

Thermodynamic properties are examined through thermodynamic parameters and they include heat capacity at constant volume (C_v), heat capacity at constant pressure (C_p), internal energy (U), enthalpy (H) and entropy (S), and Gibbs free energy (G). The significant changes in its structure are observed corresponding to variations in temperature using Moltran program [16]. The parameters characterize the direction and state of a chemical process [33]. The partition function and Boltzmann distributions are used to estimate the thermodynamic properties [48]. In this study, the standard thermodynamic properties: enthalpy (H^o_m), entropy (S^o_m) and heat capacity ($C^o_{p,m}$) of title molecule at temperature range of 50-500 K have been investigated and shown in Fig. 10. A quadratic polynomial fitting was used instead of linear or cubic models to describe the temperature dependence of thermodynamic functions, as it provides a precise representation of the system's free energy, particularly capturing explicit anharmonic effects, such as phonon-phonon interactions and the coupling of phonons with other excitation mechanisms at elevated temperatures [49]. The quadratic equations from (12) to (14) have been obtained from the second-order polynomial fit between the thermodynamic quantities (dependent variable) and the temperature (independent variable). The coefficients in the provided equations are primarily empirical fitting parameters chosen to best model the data.

$$H^o_m = 416.90082 + 0.02264\,T + 2.5913 \times 10^{-4} T^2 \tag{12}$$

$$S^o_m = 206.79517 + 0.83989\,T - 3.81673 \times 10^{-4} T^2 \tag{13}$$

$$C^o_{p,m} = 22.16545 + 0.53634\,T - 5.07897 \times 10^{-5} T^2 \tag{14}$$

The values of R^2 corresponding to quadratic relations are 0.9999, 0.99704 and 0.9993 for H^o_m, S^o_m, and $C^o_{p,m}$ respectively and these values are greater than 0.99, which indicates that they are highly correlated.

From Fig. 10, it was observed that the heat capacity increases as the temperature rises, indicating the activation of molecular degrees of freedom. On the other hand, the thermal energy content is indicated by the enthalpy and its rise reflects the accumulation of internal energy arising from increased molecular motion and vibrational excitation at elevated temperatures. But, as the temperature rises, the randomness of the system also increases. So, the entropy of the system decreases. The calculated thermodynamic parameters provide key benchmarks in the material design and offer valuable information regarding the thermal stability and energetic characteristics of the molecule, which is important for spectroscopic analysis, reaction thermodynamics, and potential pharmaceutical uses where stability at varying temperatures is essential.

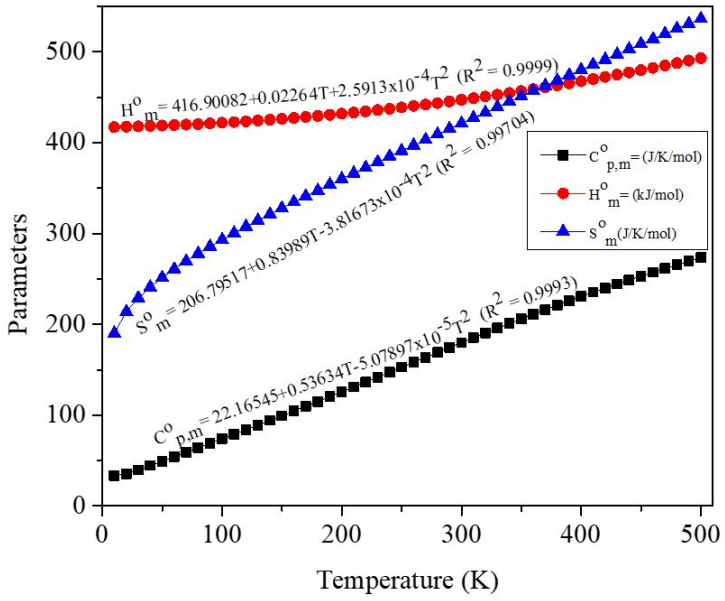

Figure 10. Correlation graph of enthalpy, entropy and heat capacity at constant pressure with varying temperature.

IV. Conclusions

This study investigates the equilibrium structure, vibrational spectra, electronic, and thermodynamic properties of herniarin using DFT at the B3LYP level with the 6-311++G(d,p) basis set. The molecule was found to be stable at a minimum energy of −16,645.48 eV (−611.71 Hartree). Calculated bond lengths, bond angles, and dihedral angles closely match experimental values. Vibrational modes corresponding to C-C, C-H, C-O, and C=O bonds exhibit strong agreement with standard infrared spectroscopy data. RDG analysis, along with ELF and LOL analyses, was performed to visualize bonding patterns, electron delocalization, and pairing tendencies, providing insights into spatial distribution and electron density localization, which are critical for understanding molecular behavior. The HOMO-LUMO gap was calculated to be 4.38 eV, consistent with the DOS results. Key global reactivity descriptors—including hardness (2.19 eV), chemical potential (−4.27 eV), softness (0.45 eV^{-1}), electronegativity (4.27 eV), and electrophilicity index (4.16 eV) were also determined. MEP and ESP surface analyses identified electron-rich regions near the oxygen atom (O16) and electron-deficient areas around hydrogen atoms, with the oxygen site exhibiting the most negative potential and the CH_3 group the highest positive potential. Mulliken charge analysis revealed that hydrogen atoms bear positive charges, while oxygen atoms carry negative charges, with C4 and C3 showing the highest positive and negative charges, respectively. Quadratic polynomial fitting was applied to model the relationships between enthalpy, heat capacity, entropy, and temperature, yielding R^2 values of 0.9999, 0.99704, and 0.9993

for H, S, and $C_{p,m}$, respectively, indicating a high degree of correlation. Overall, this work provides comprehensive data on herniarin's structural, electronic, vibrational, and thermodynamic characteristics, offering a valuable foundation for research in drug development, toxicity assessment, metabolic studies, and educational applications in biological and computational chemistry. These findings support future advancements in medicine, healthcare, and related fields.

V. Acknowledgments

We gratefully acknowledges the University Grants Commission, Nepal, for their support through the Postdoctoral Fellowship program and the Collaborative Research Grant [CRG-78/79-S&T-03]. We gratefully acknowledge the Department of Physics, St. Xavier's College, Kathmandu, for their software facility support in this study.

References

[1] Ahmad A, Misra LN. Isolation of herniarin and other constituents from Matricaria chamomilla flowers. International Journal of Pharmacognosy. 1997;35(2):121-5.

[2] Anegundi N, Pancharatna K, Pancharatna K. Evidence for antiangiogenic potentials of Herniarin (7-methoxycoumarin). Der Pharmacia Lettre. 2017;9(6):96-104.

[3] Al-Azawi KF. Preparation, Full Characterization and Theoretical Studies for New Herniarin derivatives. Engineering and Technology Journal. 2017;35(Part B, No. 1):29-32.

[4] Sun J, Han T, Yang T, Chen Y, Huang J. Interpreting the molecular mechanisms of Yinchenhao decoction on hepatocellular carcinoma through absorbed components based on network pharmacology. BioMed Research International. 2021;2021(1):6616908.

[5] Ang AM, Peteros NP, Uy MM. Antioxidant and toxicity assay-guided isolation of herniarin from Equisetum debile Roxb. (Equisetaceae). Asian Journal of Biological and Life Sciences. 2019;8(1):30-5.

[6] Hatem NA, Najah ZM. Isolation and elucidation of some chemical constituents of Lavandula officinalis. Journal of Chemical and Pharmaceutical Research. 2016;8(3):394-401.

[7] Porras-Dávila SL, Jiménez-Ferrer E, Román-Ramos R, González-Cortazar M, Almanza-Pérez JC, Herrera-Ruiz M. Herniarin, dimethylfraxetin and extracts from Tagetes lucida, in psychosis secondary to ketamine and its interaction with haloperidol. Plants. 2022;11(20):2789.

[8] Prabavathi N, Nayaki NS. Experimental Spectroscopic (FT-IR, FT-Raman, NMR) and DFT Studies of 7-methoxy-4-bromomethylcoumarin. Journal of Environmental Nanotechnology. 2014;3(2):108-21.

[9] Joseph L, Sajan D, Reshmy R, Sasi BA, Erdogdu Y, Thomas KK. Vibrational spectra, structural conformations, scaled quantum chemical calculations and NBO analysis of 3-acetyl-7-methoxycoumarin.

Spectrochimica Acta Part A: Molecular and Biomolecular Spectroscopy. 2012;99:234-47.

[10] Morais VM, Sousa CC, Matos MA. Experimental and computational study of the energetics of methoxycoumarins. Journal of Molecular Structure: THEOCHEM. 2010;946(1–3):13-9.

[11] Frisch MJ. Gaussian 09, Revision D.01. Wallingford, CT; 2009.

[12] Frisch HP, Hratchian RD, Dennington TA, Keith J, Millam AB, Nielsen A. GaussView, Version 5.08; 2009.

[13] O'Boyle NM, Tenderholt AL, Langner KM. Cclib: A library for package-independent computational chemistry algorithms. Journal of Computational Chemistry. 2008;29(5):839-45.

[14] Lu T, Chen F. Multiwfn: A multifunctional wavefunction analyzer. Journal of Computational Chemistry. 2012;33(5):580-92.

[15] Humphrey W, Dalke A, Schulten K. VMD: Visual molecular dynamics. Journal of Molecular Graphics. 1996;14:33-8.

[16] Ignatov SK. Moltran v. 2.5: Program for molecular visualization and thermodynamic calculations; 2004.

[17] Johnson ER, Keinan S, Mori-Sánchez P, Contreras-García J, Cohen AJ, Yang W. Revealing noncovalent interactions. Journal of the American Chemical Society. 2010;132(18):6498-506.

[18] Becke AD, Edgecombe KE. A simple measure of electron localization in atomic and molecular systems. The Journal of Chemical Physics. 1990;92(9):5397-403.

[19] Schmider HL, Becke AD. Two functions of the density matrix and their relation to the chemical bond. The Journal of Chemical Physics. 2002;116(8):3184-93.

[20] Magar PG, Uprety R, Rai KB. First-Principles DFT Study of the molecular structure, spectroscopic analysis, electronic structures and thermodynamic properties of Ascorbic Acid. Himalayan Physics. 2024;11:28-40.

[21] Chand S, Al-Omary FA, El-Emam AA, Shukla VK, Prasad O, Sinha L. Study on molecular structure, spectroscopic behavior, NBO, and NLO analysis of 3-methylbenzothiazole-2-thione. Spectrochimica Acta Part A: Molecular and Biomolecular Spectroscopy. 2015;146:129-41.

[22] Mir MA. DFT, Hirshfeld surface, molecular docking and drug likeness studies of medicinally important coumarin molecule. Arabian Journal for Science and Engineering. 2023;48(6):7445-62.

[23] Rai KB, Khadka IB, Koirala AR, Ray SK. Insight of cleaning, doping and defective effects on the graphene surface by using methanol. Advances in Materials Research. 2021;10(4):283-92.

[24] Krishnan AR, Saleem H, Subashchandrabose S, Sundaraganesan N, Sebastian S. Molecular structure, vibrational spectroscopic (FT-IR, FT-Raman), UV and NBO analysis of 2-chlorobenzonitrile by density functional method. Spectrochimica Acta Part A: Molecular and Biomolecular Spectroscopy. 2011;78(2):582-9.

[25] Rai KB, Khadka IB, Kim EH, Ahn SJ, Kim HW, Ahn JR. Influence of Hydrophobicity on the

Chemical Treatments of Graphene. Journal of the Korean Physical Society. 2018;72(1):107-10.

[26] Erdoğdu Y, Dereli Ö, Sarıkaya EK. Vibrational (FT-IR and FT-Raman), NMR and quantum chemical investigations on 7-Methylcoumarin. Journal of Spectroscopy and Molecular Sciences. 2020;2(2):51-64.

[27] Bishwokarma N, Budha C, Teemilsina NK, Rai KB. Exploring vibrational spectra, electronic properties and thermal analysis of Isoguanine molecule using DFT. Scientific World. 2025;18(18):5-14.

[28] Park JW, Shumaker-Parry JS. Structural study of citrate layers on gold nanoparticles: Role of intermolecular interactions in stabilizing nanoparticles. Journal of the American Chemical Society. 2014;136(5):1907-21.

[29] Turner MJ, Grabowsky S, Jayatilaka D, Spackman MA. Accurate and efficient model energies for exploring intermolecular interactions in molecular crystals. The Journal of Physical Chemistry Letters. 2014;5(24):4249-55.

[30] Janani S, Rajagopal H, Muthu S, Aayisha S, Raja M. Molecular structure, spectroscopic (FT-IR, FT-Raman, NMR), HOMO-LUMO, chemical reactivity, AIM, ELF, LOL and molecular docking studies on 1-Benzyl-4-(N-Boc-amino) piperidine. Journal of Molecular Structure. 2021;1230:129657.

[31] Savin A. The electron localization function (ELF) and its relatives: Interpretations and difficulties. Journal of Molecular Structure: THEOCHEM. 2005;727(1–3):127-31.

[32] Savin A, Nesper R, Wengert S, Fässler TF. ELF: The electron localization function. Angewandte Chemie International Edition in English. 1997;36(17):1808-32.

[33] Manickavelu M, Govindrajan B, Sambantham M, Panneerselvam P, Irfan A. Computational investigation of effects of polar and non-polar solvents on optimized structure with topological parameters (ELF, LOL, AIM, and RDG) of three glycine derivative compounds. Structural Chemistry. 2022;33(4):1295-319.

[34] Jacobsen H. Localized-orbital locator (LOL) profiles of chemical bonding. Canadian Journal of Chemistry. 2008;86(7):695-702.

[35] Rajalakshmi K, Vetrivel M. NBO and topology (MESP, ELF, LOL) analysis of 2-hydroxypropanamide. International Journal. 2020;5:50-8.

[36] Govindasamy P, Gunasekaran S, Srinivasan S. Molecular geometry, conformational, vibrational spectroscopic, molecular orbital and Mulliken charge analysis of 2-acetoxybenzoic acid. Spectrochimica Acta Part A: Molecular and Biomolecular Spectroscopy. 2014;130:329-36.

[37] Sworakowski J. How accurate are energies of HOMO and LUMO levels in small-molecule organic semiconductors determined from cyclic voltammetry or optical spectroscopy? Synthetic Metals. 2018;235:125-30.

[38] Budha C, Rai KB. Study of the molecular structure, spectroscopic analysis, electronic structures and thermodynamic properties of Niacin molecule using first-principles. Journal of Nepal Chemical

Society. 2024;44(2):1-12.

[39] Khalili F, Vafaee M, Cho D, Shokri B. Charge migration in caffeine: A real-time time-dependent density functional theory study. International Journal of Quantum Chemistry. 2021;121(19):e26754.

[40] Abraham CS, Prasana JC, Muthu S, Raja M. Quantum computational studies, spectroscopic (FT-IR, FT-Raman and UV–Vis) profiling, natural hybrid orbital and molecular docking analysis on 2,4-dibromoaniline. Journal of Molecular Structure. 2018;1160:393-405.

[41] Uprety R, Ghimire R, Magar PG, Rokka D, Khadka IB, Neupane R, et al. Study of the molecular structure, electronic structure, spectroscopic analysis and thermodynamic properties of dibenzofuran using first principles. Journal of Nepal Physical Society. 2024;10(2):8-18.

[42] Eryılmaz S. The theoretical investigation of global reactivity descriptors, NLO behaviours and bioactivity scores of some norbornadiene derivatives. Sakarya University Journal of Science. 2018;22(6):1638-47.

[43] Mathammal R, Sangeetha K, Sangeetha M, Mekala R, Gadheeja S. Molecular structure, vibrational, UV, NMR, HOMO-LUMO, MEP, NLO, NBO analysis of 3,5-di-tert-butyl-4-hydroxybenzoic acid. Journal of Molecular Structure. 2016;1120:1-4.

[44] Basnet B, Magar AR, Ghimire R, Joshi U, Rai KB. First-principles calculations to investigate structural, spectroscopic features, electronic and thermodynamic properties of trichloroacetaldehyde. Himalayan Journal of Science and Technology. 2024;8(1):1-9.

[45] Bakheit AH, Al-Salahi R, Al-Majed AA. Thermodynamic and computational (DFT) study of non-covalent interaction mechanisms of charge transfer complex of linagliptin with 2,3-dichloro-5,6-dicyano-1,4-benzoquinone (DDQ) and chloranilic acid (CHA). Molecules. 2022;27(19):6320.

[46] Lakshminarayanan S, Jeyasingh V, Murugesan K, Selvapalam N, Dass G. Molecular electrostatic potential (MEP) surface analysis of chemo sensors: An extra supporting hand for strength, selectivity and non-traditional interactions. Journal of Photochemistry and Photobiology. 2021;6:100022.

[47] Rai KB, Teemilsina NK, Siwakoti B. First principles study of structural equilibrium configuration of ortho-, meta-, and para-chloroaniline molecules. Scientific World. 2024;17(17):7-18.

[48] Singh S, Singh H, Karthick T, Agarwal P, Erande RD, Dethe DH, et al. Combined experimental and theoretical investigation on an alkaloid–dimethylisoborreverine. Journal of Molecular Structure. 2016;1103:187-201.

[49] Jung JH, Srinivasan P, Forslund A, Grabowski B. High-accuracy thermodynamic properties to the melting point from ab initio calculations aided by machine-learning potentials. Computational Materials. 2023;9:3.